Lin *et al.*
Chinese Journal of Mechanical Engineering (2024) 37:102
https://doi.org/10.1186/s10033-024-01088-4

Chinese Journal of Mechanical Engineering

ORIGINAL ARTICLE

Open Access

Laser Powder Bed Fusion of Multifunctional Bio-inspired Vertical Honeycomb Sandwich Structures: For the Application of Lightweight Bipolar Plates of Proton Exchange Membrane Fuel Cells

Kaijie Lin[1,2], Yong Xu[1,2], Dongdong Gu[1,2*], Junhao Shan[1,2], Keyu Shi[1,2] and Wanli Zhang[1,2]

Abstract

The bipolar plate (BPP) is a crucial component of proton exchange membrane fuel cells (PEMFC). However, the weight of BPPs can account for around 80% of a PEMFC stack, posing a hindrance to the commercialization of PEMFCs. Therefore, the lightweight design of BPPs should be considered as a priority. Honeycomb sandwich structures meet some requirements for bipolar plates, such as high mechanical strength and lightweight. Animals and plants in nature provide many excellent structures with characteristics such as low density and high energy absorption capacity. In this work, inspired by the microstructures of the Cybister elytra, a novel bio-inspired vertical honeycomb sandwich (BVHS) structure was designed and manufactured by laser powder bed fusion (LPBF) for the application of lightweight BPPs. Compared with the conventional vertical honeycomb sandwich (CVHS) structure formed by LPBF under the same process parameters setting, the introduction of fractal thin walls enabled self-supporting and thus improved LPBF formability. In addition, the BVHS structure exhibited superior energy absorption (EA) capability and bending properties. It is worth noting that, compared with the CVHS structure, the specific energy absorption (SEA) and specific bending strength of the BVHS structure increased by 56.99% and 46.91%, respectively. Finite element analysis (FEA) was employed to study stress distributions in structures during bending and analyze the influence mechanism of the fractal feature on the mechanical properties of BVHS structures. The electrical conductivity of structures were also studied in this work, the BVHS structures were slightly lower than the CVHS structure. FEA was also conducted to analyze the current flow direction and current density distribution of BVHS structures under a constant voltage, illustrating the influence mechanism of fractal angles on electrical conductivity properties. Finally, in order to solve the problem of trapped powder inside the enclosed unit cells, a droplet-shaped powder outlet was designed for LPBF-processed components. The number of powder outlets was optimized based on bending properties. Results of this work could provide guidelines for the design of lightweight BPPs with high mechanical strength and high electrical conductivity.

Keywords Lightweight bipolar plates, Bio-inspired honeycomb sandwich structures, Laser powder bed fusion, Forming quality, Bending properties, Electrical conductivity

*Correspondence:
Dongdong Gu
dongdonggu@nuaa.edu.cn
Full list of author information is available at the end of the article

1 Introduction

With the continuous decrease of the world's fossil fuel resources and the increasing demand for global energy, the need for clean energy is becoming more prevalent. Proton exchange membrane fuel cells (PEMFC) have the potential to meet this demand [1]. The bipolar plate (BPP) is one of the most important components in PEMFCs, the weight/mass of BPPs can account for around 80% of a PEMFC stack. Hence, lightweight design of the BPP should be considered to achieve higher power density [2, 3]. Meanwhile, the BPP has to meet other requirements such as high mechanical strength and high electrical conductivity. Sandwich structures fulfill requirements for bipolar plates due to their high specific strength and specific energy absorption (SEA). A typical sandwich structure consists of outer panels and a core embedded between them, while various alternative core designs have been employed, including truss core [4–6], foam core [7, 8], honeycomb core [9], corrugated core [10–12], bio-inspired core [13, 14], etc. Conventional manufacturing methods generally connect the panel and the core together by bonding or welding, which not only increases the weight of the sandwich structure but also results in lower structural strength [15]. Laser additive manufacturing (LAM) is an advanced manufacturing technology based on layer-by-layer forming principle, which can be used to manufacture complex structural components [16, 17]. Recently, laser powder bed fusion (LPBF) is a rapidly developing LAM technology [18, 19], and it uses a fine laser beam with high energy density to selectively fuse regions of a powder bed [20]. LPBF is suitable for direct printing of complex structures due to its high manufacturing precision [21] and it provides high design freedom and forming flexibility for the manufacture of complex sandwich cores [22–25].

In nature, animals and plants provide numerous excellent structures with characteristics such as low density, high strength and high energy absorption capacity [26–28]. Therefore, the biomimetic method is a potential way for designing high-performance sandwich structures. Researchers have increasingly used the biomimetic method to design new sandwich cores with excellent mechanical properties in recent years. One of the typical sandwich core structures is the lattice truss core, and it has attracted wide attention. For example, Ullah et al. [29] found that bio-inspired kagome truss sandwich structures formed by LPBF had superior compressive and shear strengths. Wang et al. [30] proved that bionic lattice structures had higher energy absorption performance than BCC lattice structures. Inspired by beetle's front wing, Wang et al. [31] proposed a bio-inspired crashworthy lattice structure and manufactured by LPBF. Results showed that bio-inspired structure exhibited a promising prospect for impact resistant applications. Although great interest has been taken in LPBF bio-inspired lattice structures, the main problem of lattice structures is that unmelted powder adhered on overhanging area of inclined rods, resulting in low forming accuracy of the as-fabricated rod [32], and is detrimental to the strength and stiffness of structures [33]. Some researchers proposed bionic thin-walled sandwich structures because of their high mechanical properties. Meng et al. [34] designed bio-inspired horizontal hollow column sandwich structures with different core heights based on Cybister elytra and produced them by LPBF, and investigated the effect of core height on the energy absorption of the sandwich structures. Results showed that the structures with core height of 6 mm exhibited the best energy absorption performance. Furthermore, Hu et al. [35] inspired by the microstructures of the Norway spruce stem, four sandwich structures with a different arrangement of horizontal hollow tubes were designed and manufactured by LPBF. Results indicated that the gradient structure, with tube size gradually decreasing from the top and bottom plate towards the center, exhibited the highest specific absorption energy, ultimate strength and specific strength. Obadimu et al. [36] investigated the compression performance of horizontal honeycomb structures manufactured by LPBF, and the deformation mode of structures was confirmed. However, in the aforementioned horizontal thin-walled core sandwich structures, the thin-walled was perpendicular to the loading direction. Thus, thin-walled cores were easily deformed under loading, and thus little energy absorption was obtained [37].

Among all sandwich structures with various bionic thin-walled cores, the vertical honeycomb core has received much attention due to the features of high energy absorption and high rigidity. For instance, Lin et al. [38] designed a novel vertical honeycomb structure with twisted feature and manufactured by LPBF. The influence of twist angle on the manufacturability and compressive behavior was studied. The results showed material relative density of LPBF-processed components was reduced with the increase of twist angle, and honeycomb structures with 30° twist angle exhibited the highest specific compressive strength and energy absorption ability. Xia et al. [39] designed a bio-inspired vertical honeycomb structure and manufactured by LPBF. The experiment results showed that structures exhibited superior energy absorption under the compression. In another study, Anandan et al. [40] manufactured vertical hexagonal honeycomb structures by LPBF and investigated the behavior of structures under loading. Results showed that failure occurred through a plastic buckling mechanism. Although above studies proved that the

vertical honeycomb cores had excellent mechanical properties, there were little reports about LPBF integrally formed vertical honeycomb cores and panels. The main problem in LPBF-processing vertical honeycomb sandwich structures is that the top panel has poor formability because of the unmelted powder bonded on overhanging area, so the internal vertical honeycomb filling core need to be optimized. In addition, the problem of unmelted powder trapped inside the enclosed unit cells should be considered [41].

Thus, aiming to improve the LPBF formability of conventional vertical honeycomb sandwich (CVHS) structures, a novel bio-inspired vertical honeycomb sandwich (BVHS) structure was designed based on microstructural features of Cybister elytra, and manufactured by LPBF for the application of lightweight BPPs. The forming quality, bending properties and electrical conductivity properties of LPBF-processed BVHS components were studied. Furthermore, the stress distribution of structures during bending and current density distribution under a constant voltage were clarified by the finite element analysis (FEA). Finally, in order to remove unmelted powder trapped inside the enclosed unit cells, a self-supported droplet-shaped powder outlet was designed and the number of powder outlets was optimized.

2 Materials and Methods

2.1 Bio-inspired Honeycomb Cells and Sandwich Structures Design

The superior mechanical properties of the Cybister elytra indicate that its special structure is an ideal prototype for protection. The Cybister elytra is a typical sandwich structure, which consists of outer skins and fiber bundles embedded between them, as shown in Figure 1(a) [34]. The black rectangle on the cross-sectional SEM images shows fractal feature of fiber bundles. The BVHS structures in this work were inspired from the fractal feature, and five bio-inspired honeycomb cells with fractal angles of 30°, 45°, 60°, 75° and 90° between fractal walls and a horizontal plane were designed (Figure 1(b)). The cell with fractal angle of 90° was the conventional honeycomb cell. Fractal wall thickness and fractal height were set as 0.75 mm and 1.2 mm. The unit cell wall thickness and unit cell size can also significantly affect performances of the honeycomb structures. In order to obtain optimized values of honeycomb cell, a series of CVHS components with seven sets of different honeycomb wall thicknesses (T) and unit cell size (L) were manufactured by LPBF, where T represented the sum of two unit cells wall thicknesses (Figure 1(c)). The optimization results of honeycomb unit cell were presented in Section 3.1. Considering the dimension of bipolar plates and mechanical testing samples, other structural parameters, including panel thickness, core height, component length, width and height, were constantly set as 1.5 mm, 2 mm, 35 mm, 5 mm and 5 mm, respectively (Figure 1(d)).

2.2 LPBF Manufacturing Process and Material

The gas atomized 316L stainless steel powder was used as the raw material for LPBF processing in this work. The LPBF system used in this work mainly consisted of a YLR-500-WC ytterbium fiber laser (IPG Laser GmbH, Germany), a powder spreading device, an inert argon gas protection system, and an automatic processing control system. The maximum power of the laser can reach 500 W, and the spot diameter is 70 μm. Based on the previous study on LPBF of 316L stainless steel [42], the main LPBF process parameters applied in this work were set as follows: laser power = 300 W, laser scanning speed = 1500 mm/s, powder layer thickness = 30 μm and hatch spacing = 50 μm.

2.3 Experiments and Performance Metrics

After grinding and polishing processes, the cross-sectional morphology of the LPBF-processed sandwich component was observed by an optical microscope (OM, PMG3, Olympus, Japan). By comparing with the CAD model in the identical area, the area of deviation can be measured by Image J and used to assess the forming accuracy of LPBF-processed sandwich components.

The three-point bending test was conducted on a 100 kN electromechanical universal testing machine (MTS Systems, CMT-5205) to evaluate the bending behavior of components, as displayed in Figure 2(a). The top faces of components were ground before bending test. The span of the support and the diameter of the indenter were 20 mm and 4 mm, respectively (Figure 2(a)). The displacement load was applied to the structures by an indenter with the rate of 2 mm/min. During the three-point bending test, the deformation process of components was recorded by a digital video (Sony, HDR-CX170) to further investigate the fracture mechanism. According to the force-displacement curves, energy absorption (EA) can be calculated by the following equation:

$$EA(e) = \int_0^{e_0} F \, \mathrm{d}e, \tag{1}$$

where F is the instantaneous force and e_0 is the deformation distance. The specific energy absorption (SEA) is the EA per unit mass (m) and it can be calculated as follows:

$$SEA(e) = \frac{EA(e)}{m}. \tag{2}$$

In addition, the bending strength (σ), was also obtained from the force-displacement curves, and can be used to assess the capability of structures to resist bending

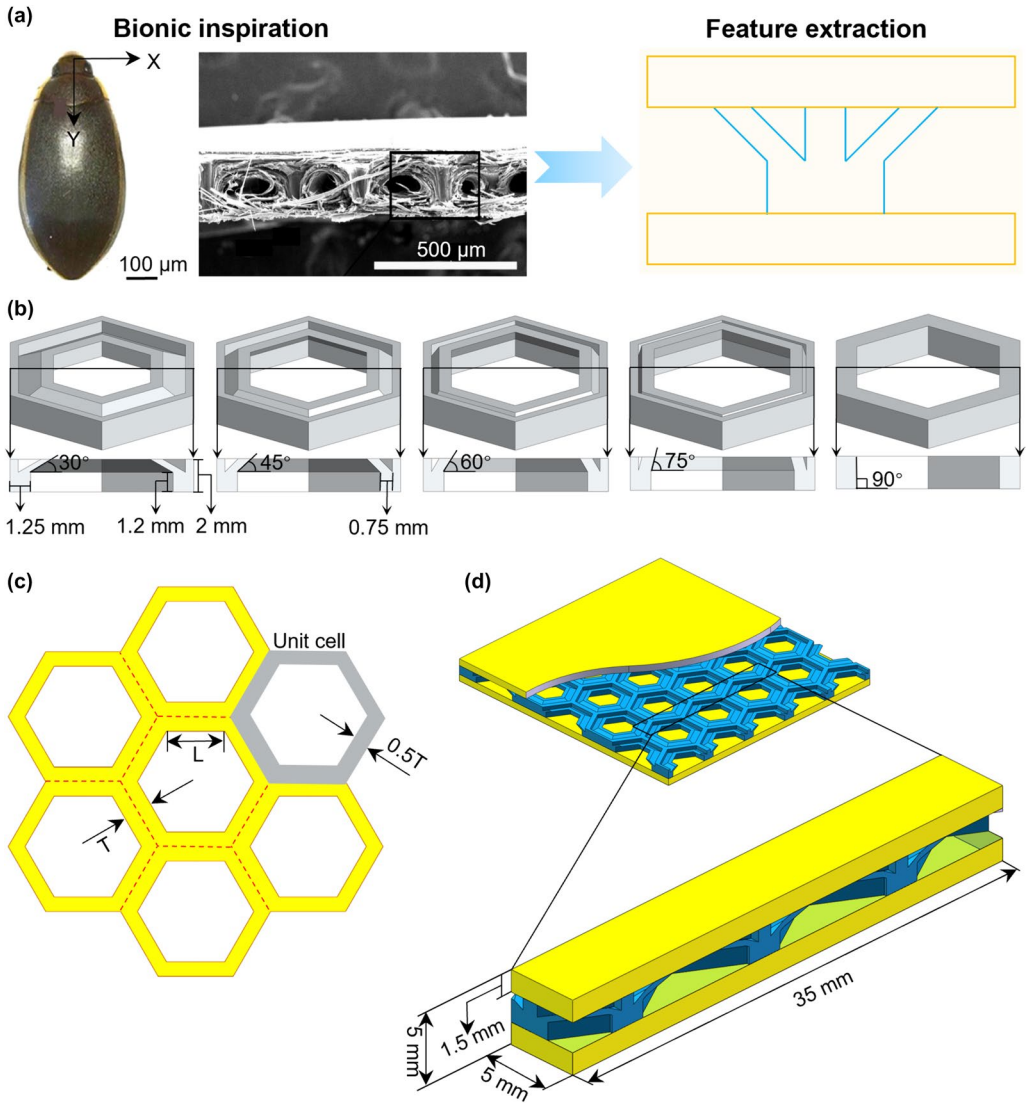

Figure 1 The design of BVHS structures: (**a**) Bionic inspiration from the microstructure Cybister elytra [34], (**b**) CAD models of bio-inspired honeycomb cells with different fractal angles, (**c**) Design parameters of the conventional honeycomb, (**d**) Design parameters of LPBF-processed bionic sandwich structures

deformation. The bending strength can be calculated by the following equation:

$$\sigma = \frac{3P \times L}{2b \times h^2}, \tag{3}$$

where P is the ultimate bending load, L is the span of the support, b is the width of samples and h is the thickness of samples. Moreover, the specific bending strength (σ_s), the bending strength (σ) per unit mass (m), was proposed in our study and can be calculated as follows:

$$\sigma_s = \frac{\sigma}{m}. \tag{4}$$

The electrical resistance was obtained with a DC resistance testing instrument (Anbai, AT516L) to evaluate the electrical conductivity of components (Figure 2(b)). Prior to the resistance testing, the top and bottom surfaces of components were polished and coated with gold to minimize the effect of interfacial contact resistance between the component and the carbon paper. The illustration in Figure 2(b) showed the resistance test device. Two pieces of carbon paper were sandwiched between the BVHS component and gold-plated copper electrodes. A constant electrical current was applied via the two copper electrodes. The compaction force applied on the two

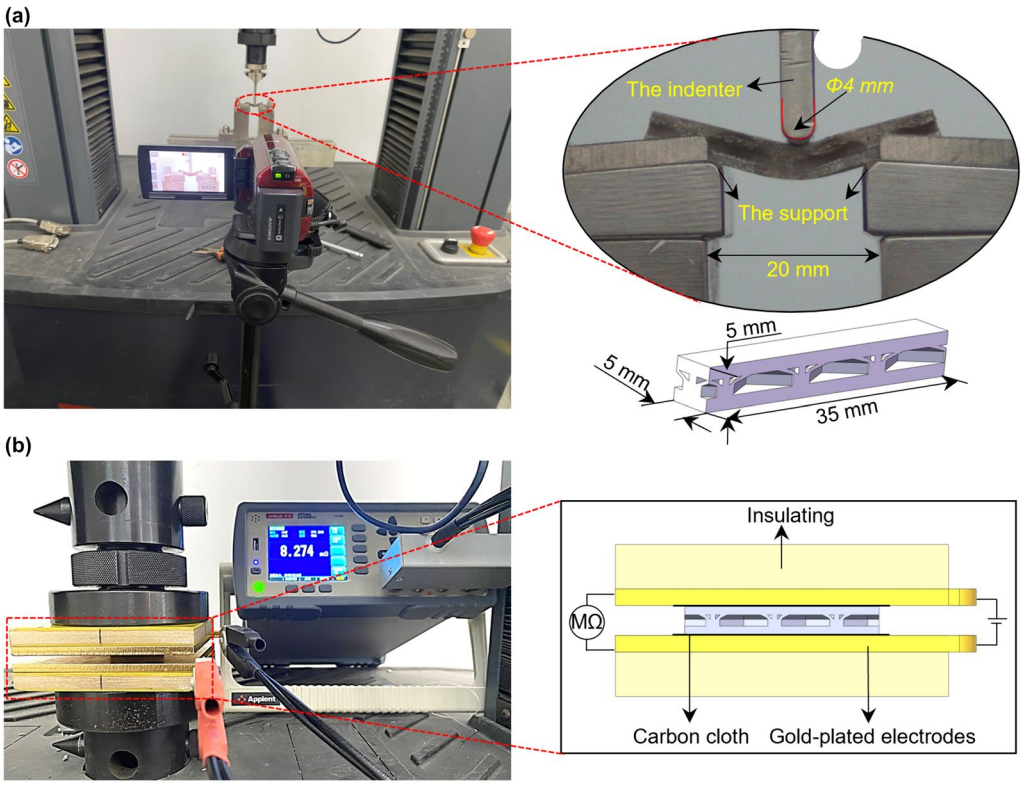

Figure 2 Images of experiment tests: (**a**) The three-point bending tests, (**b**) The resistance tests

insulating resin boards was provided by an electromechanical universal testing machine (MTS Systems, CMT-5205). With increasing pressure, the value of resistance was recorded until the reading on the DC resistance testing instrument stabilized. The bulk resistance of LPBF-processed components can be calculated as follows:

$$R = R_{BP} + R_G + R_C + R_{CR}, \tag{5}$$

where R is the electrical resistance value recorded by a DC resistance testing instrument, R_{BP} is the bulk resistance of samples, R_{BP} is the bulk resistance of the gold-plated copper electrodes, R_C is the bulk resistance of the carbon paper, R_{CR} is the sum of interfacial contact resistance between the gold-plated copper electrodes and the carbon paper, the carbon paper and the components. In addition, R_G, R_C and R_{CR} were regarded as constant, hence their influence on the test results was not considered in this experiment. In this work, R was used as a metric to evaluate the electrical conductivity properties of LPBF-processed honeycomb components.

2.4 Finite Element Analysis

The numerical simulation of structures under three-point bending was conducted by ANSYS LS-DYNA to analyze the stress distribution and deformation process. The indenter and the support were replaced with three rigid rods to simplify the model (Figure 3(a)), which can improve the computation speed of numerical simulation. During the simulation, the bottom rods were fixed, the top rod was constrained by a displacement of 15 mm along the coordinate system $-Z$ direction. Besides, the distance between the bottom rods were set as 20 mm. Friction was used as the contact mode of whole models and the friction coefficient was 0.30. The stress–strain curve of the 316L stainless steel sample and material properties were shown in Figure 3(b).

The numerical simulation of current density distribution of honeycomb sandwich structures was conducted by COMSOL. The equation underlying the solution of the model is the charge conservation equation, which can be calculated as follows:

$$\nabla \cdot (-\sigma V) = 0, \tag{6}$$

where ∇ is the gradient operator, σ is the material conductivity and V is the potential. A conductivity of 13100 S/cm was obtained for the LPBF-processed 316L stainless steel using a metal four-probe tester (RTS-11), which was then input into COMSOL as a material parameter. As shown in Figure 3(c), Dirichlet boundary conditions were set on the top and bottom surfaces of the model,

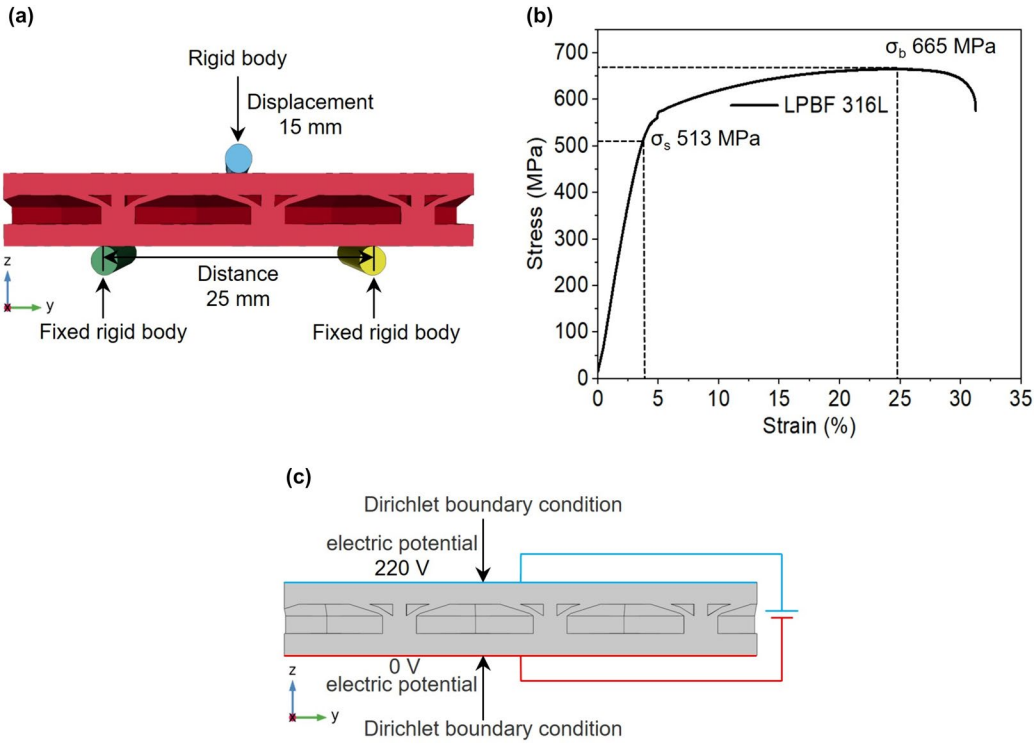

Figure 3 (**a**) Numerical simulation of three-point bending, (**b**) The uniaxial tensile stress–strain curve of 316L at room temperature, (**c**) Numerical simulation of electrical conductivity properties

where a constant potential of 220 V was applied to the top surface and a constant potential of 0 V was applied to the bottom surface. The current density distribution was studied by selecting a *YZ* plane at an identical position.

3 Results and Discussion

3.1 Optimization of the Honeycomb Unit Cell Size

Seven structures with different sets of honeycomb wall thicknesses (T) and unit cell size (L) were fabricated by LPBF and compared according to three performance criteria, namely light-weighting, flexural strength and electric conductivity. LPBF-processed CVHS components were shown in Figure 4. The weight of seven LPBF-processed CVHS components and a solid LPBF-processed component with the same sample size were obtained by an electronic balance (Xing Yun, JA103P), and the performance criteria of light-weighting was calculated as follows:

$$m_l = (m_s - m_c)/m_s, \tag{7}$$

where m_l is light-weighting, m_s is the weight of the solid component, m_c is the weight of the CVHS component. For the performance criteria of flexural strength and electrical conductivity, which was obtained by the three-point bending test and the DC resistance testing,

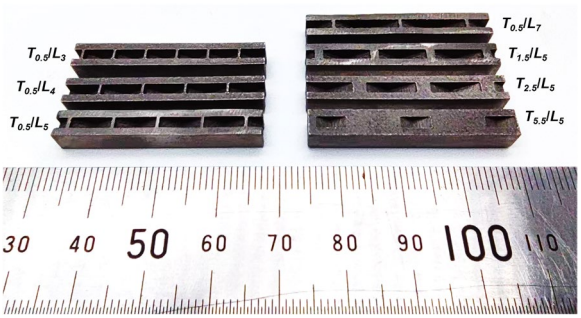

Figure 4 LPBF-processed CVHS components with different sets of honeycomb wall thicknesses (T) and unit cell size (L)

respectively. It is worth noting that the electrical conductivity should be obtained by the following equation:

$$S_c = \frac{1}{R}, \tag{8}$$

where S_c is electrical conductivity, R is the electrical resistance value recorded by the DC resistance testing instrument. The results of three performance criteria of CVHS components were shown in Table 1 and drawn in Figure 5(a). According to Figure 5(a), triangle area proportions of seven components were calculated

Table 1 Three performance criteria of CVHS components with different structural parameter

Structural parameter	Light-weighting (%)	Flexural strength (MPa)	Electrical conductivity (S/cm)
$T_{0.5}/L_3$	31.58	1072	9.32
$T_{0.5}/L_4$	33.12	1042	10.03
$T_{0.5}/L_5$	33.54	1023	10.99
$T_{0.5}/L_7$	33.62	898	8.5
$T_{1.5}/L_5$	23.34	1284	11.6
$T_{2.5}/L_5$	15.95	1428	11.9
$T_{5.5}/L_5$	3.169	1651	12.99

and charted in Figure 5(b) to assess the overall performance of the CVHS components. The results showed that $T_{2.5}/L_5$ exhibited the highest area proportion and the best overall performance. Therefore, the thickness of 2.5 mm and unit cell size of 5 mm were used for further investigation.

3.2 Forming Quality of BVHS Components

LPBF-processed BVHS components with different fractal angles (30°, 45°, 60°, 75° and 90°) and corresponding CAD models were shown in Figure 6. From images of the LPBF-processed components, hanging dross with different amount can be clearly observed on the lower surface of the top panel of different components (marked by red arrows). Without solid-supporting structures, the liquid metal in the laser-induced melt pool tended to permeate downward into gaps among powder bed, resulting in the formation of dross [43]. Figure 7(a) showed LPBF-processed components with different fractal angles (30°, 45°, 60°, 75°, 90°) and OM images of selected cells, where the red dashed line represented the designed profile. It can be found that the irregular-shaped profile, which was formed for the reason of hanging dross, can be observed on overhanging area. While the 90° component exhibited the most irregular profile, which significantly decreased the dimension accuracy. For other four components, with the decrease of the fractal angle, the processed profile was gradually smoothed. To quantitatively compare the

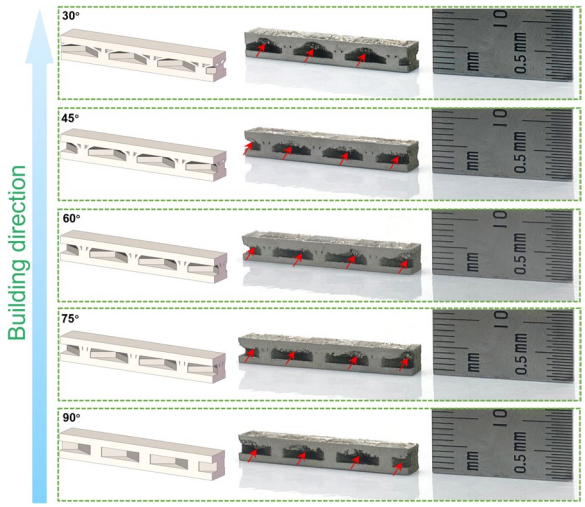

Figure 6 The BVHS structures manufacturing by laser powder bed fusion with different fractal angles: 30°, 45°, 60°, 75° and 90°

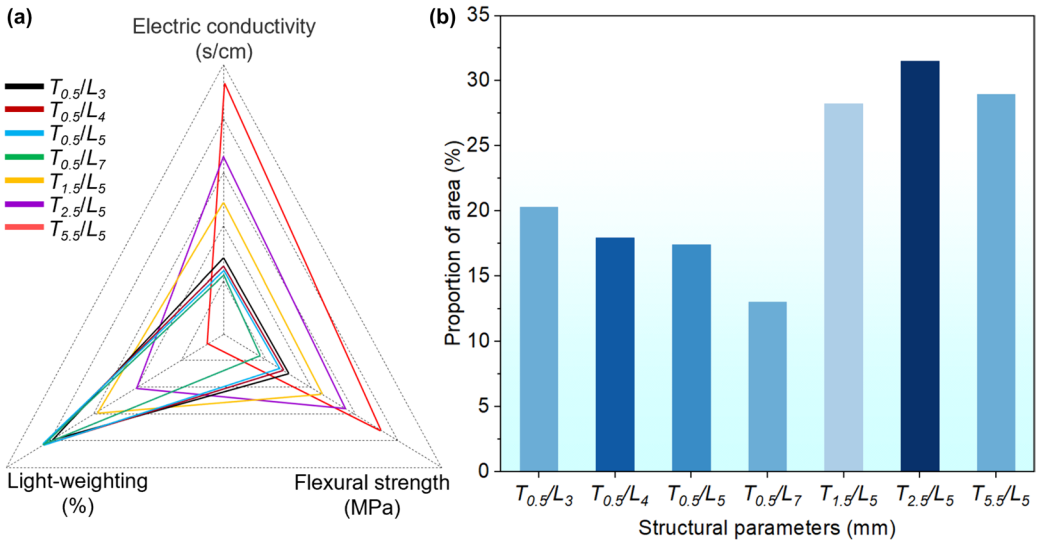

Figure 5 The parameters optimization of the CVHS structure: (**a**) Performance evaluation of seven structural parameters based on three performance criteria: electric conductivity, light-weighting and flexural strength, (**b**) Area proportion of the seven structural parameters

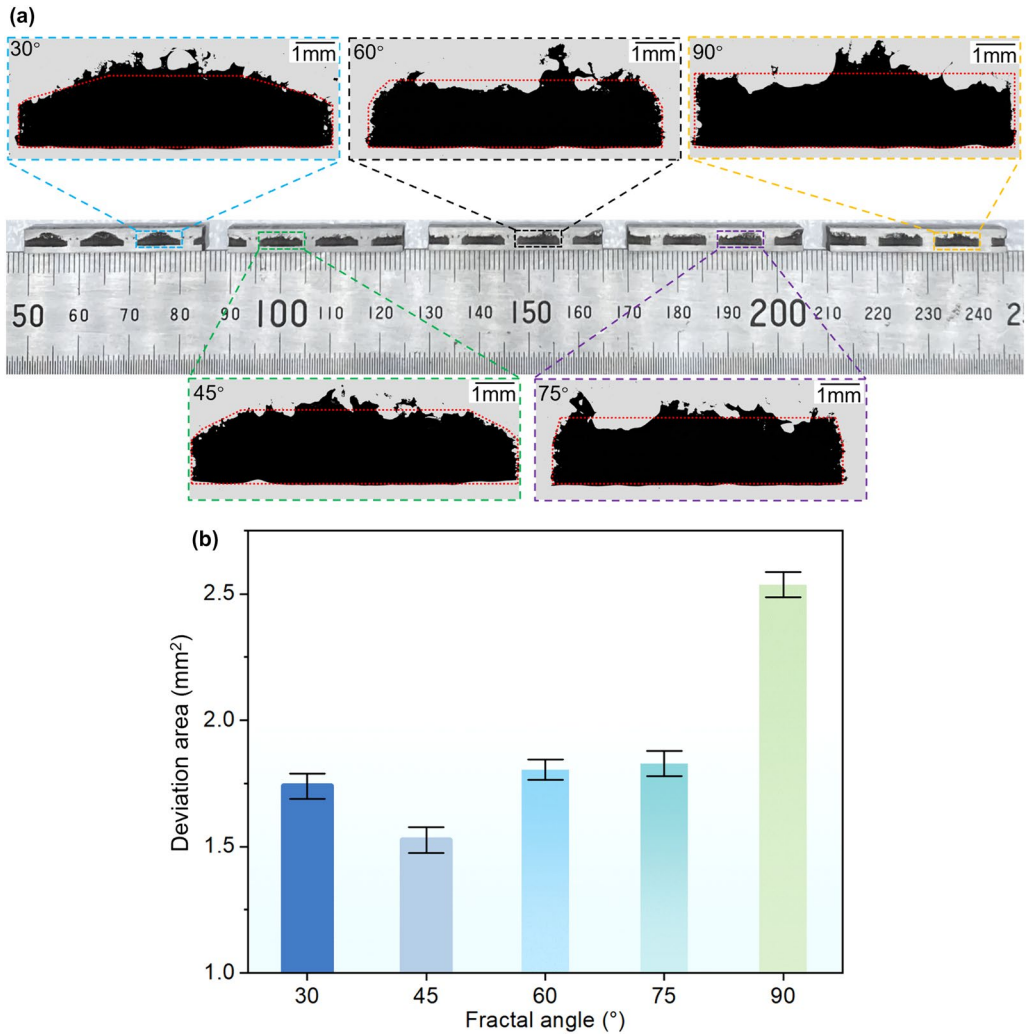

Figure 7 OM micrographs and manufacturing accuracy of the LPBF-processed BVHS components: (**a**) Images of the overhanging area, (**b**) Manufacturing accuracy of components

formability of five components, the sum of cross-section area inside the design profile and the vacant area between the design profile and the cross-section was used to assess formability. The deviation area of five components with different fractal angles (30°, 45°, 60°, 75°, 90°) were shown in Figure 7(b). It can be seen that the 45° component showed the minimum deviation area (1.53 mm^2), thus its manufacturing accuracy is the highest, followed by the 30° component (1.74 mm^2), the 60° component (1.80 mm^2), the 75° component (1.83 mm^2) and the 90° component (2.54 mm^2). Compared to the other four components, the 90° component exhibited the poorest formability, which was due to the largest overhang area dimension of the top panel. The introduction of fractal features reduced the overhang area dimension of the top panel and thus improved the formability of other four components. For other four LPBF-processed BVHS components with different fractal angles (30°, 45°, 60° and 75°), the overhang area dimension of the top panel generally decreased with decreasing fractal angles. However, the 45° component had the highest manufacturing accuracy, followed by the 30° component, the 60° component, the 75° component. This because for fractal thin walls, its inclined lower surfaces also negatively affected formability of LPBF-processed components [44]. Although the 30° component had the smallest overhang area dimension of the top panel, the fractal thin walls lacked sufficient support during LPBF processing, resulting in a larger area of deviation. For the 45° component, due to self-support behavior, the processed profile of the fractal thin walls was well consistent with the designed profile, so it had the minimum area of deviation, namely the best formability.

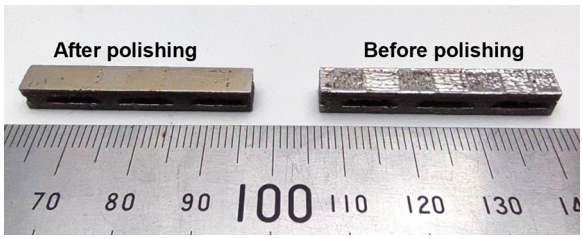

Figure 8 Comparison of bending specimens before and after polishing

3.3 Mechanical Properties and Deformation Process

Prior to the three-point bending experiment, the top faces of the samples were polished as shown in Figure 8. The representative force–displacement curves of five BVHS components under three-point bending tests were shown in Figure 9(a). It can be seen that the curve of the 75° component can be divided into three regions, namely a linear elastic deformation region, a plastic deformation region and a force drop region. While curves of other four components exhibited a similar trend and included four regions, namely a linear elastic deformation region, a plastic deformation region, a plateau region and a force drop region. From the comparison of force–displacement curves, it can be seen that the 90° component exhibited the smallest elastic displacement (0.06 mm), followed by the 75° component (0.08 mm), the 60° component (0.13 mm), the 30° component (0.14 mm) and the 45° component (0.17 mm). However, the 30° component exhibited the highest ultimate bending force (5.15 kN) in the plastic deformation region, which was 0.76%, 12.44%, 18.87% and 32.49% higher than the 45° component (5.11 kN), the 75° component (4.51 kN), the 60° component (4.18 kN) and the 90° component (3.48 kN). In addition, the 30° component exhibited the largest displacement (4.96 mm) at the ultimate bending force, followed by the 75° component (4.88 mm), the 90° component (4.81 mm), the 45° component (4.51 mm) and the 60° component (4.35 mm). After the plastic deformation region, the 90° component experienced the longest plateau region (2.95 mm), followed by the 45° component (2.53 mm), the 60° component (2.34 mm) and the 30° component (2.18 mm). Finally, all curves entered force drop region with the increase of the displacement. It is worth noting that none of the five components experienced fracture during the three-point bending process, which can be attributed to the excellent toughness of 316L stainless steel.

Figure 9(b) showed the *SEA* and specific flexural strength (σ_s) of the five LPBF-processed BVHS components based on the three-point bending force-displacement curves. The 30° component (10.55 J/g, 238.11 MPa/g) and the 45° component (10.54 J/g, 233.04 MPa/g) exhibited relatively higher *SEA* and specific flexural strength, followed by the 60° component (8.52 J/g, 205.96 MPa/g), the 75° component (8.65 J/g, 200.87 MPa/g). The 90° component (6.72 J/g, 161.86 MPa/g) exhibited the

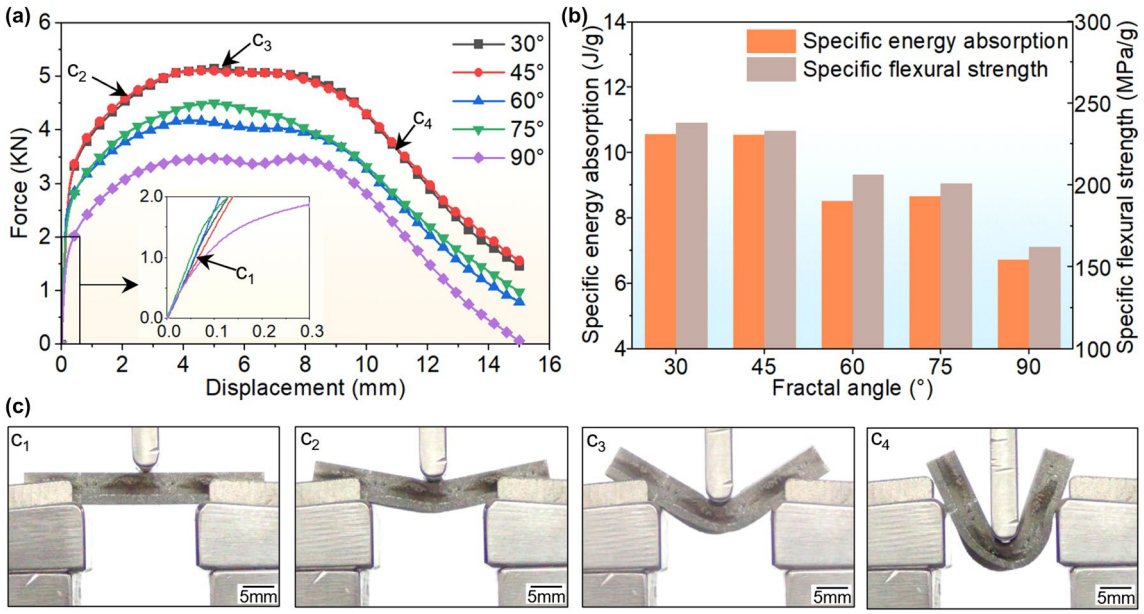

Figure 9 Bending properties of BVHS components fabricated by LPBF: (**a**) The force-displacement bending curves, (**b**) The specific energy absorption and specific flexural strength of LPBF-processed BVHS components, (**c**) The snapshots of four typical stages of the 30° component marked in (**a**)

lowest *SEA* and specific flexural strength. From the above comparison, it can be seen that with the increase of the fractal angle, the mechanical properties of the structures obviously decreased. Figure 9(c) showed four snapshots obtained during the three-point bending test of the 30° component, captured from the elastic deformation region (c1 in Figure 9(a)), the plastic deformation region (c2 in Figure 9(a)), the plateau region (c3 in Figure 9(a)) and the force drop region (c4 in Figure 9(a)), respectively. When the component deformed to the force drop region (Figure 9(c4)), the component slid on the support, which resulting in the decrease of bending forces.

The influence of fractal angles on the mechanical properties of BVHS structures was illustrated by FEA. Figure 10(a), (b) showed the stress distribution results of the 90° structure and the 30° structure when reaching the ultimate bending force. The insets in Figure 10(a), (b) showed the stress distribution at the same position of different structures. By comparing the stress distribution of the bottom view of the 30° structure and 90° structure, it can be seen that the stress of two structures mostly concentrated around central area of the bottom panel, but the stress concentration area (marked by black circle) of the 90° structure was significantly larger than the 30° structure. From the front view, it can be seen that the inner vertical honeycomb wall of the 90° structure had local stress concentration area (marked by a white circle and an arrow), while the 30° structure exhibited uniform stress distribution at the same position. To further investigate the influence of fractal features on the stress distribution of structures, the 30° structure and the 90° structure at the fractal position (marked by a black dashed rectangle) were extracted to exhibit the stress distribution in detail. For the 90° structure, the stress was mainly concentrated in the top panel, while the vertical honeycomb wall showed the uniform stress distribution. For the 30° structure, the top panel still bore most of the bending force, but the fractal thin wall existed the local stress concentration area (marked by red dashed line). It can be concluded that the local stress concentration occurred at the fractal thin wall during bending, the transmission of force was hindered. Therefore, the introduction of the fractal thin wall obstructed the transmission of force and dissipated most of the force, leading to more uniform distribution of stress across the structure, and thus improving the mechanical properties.

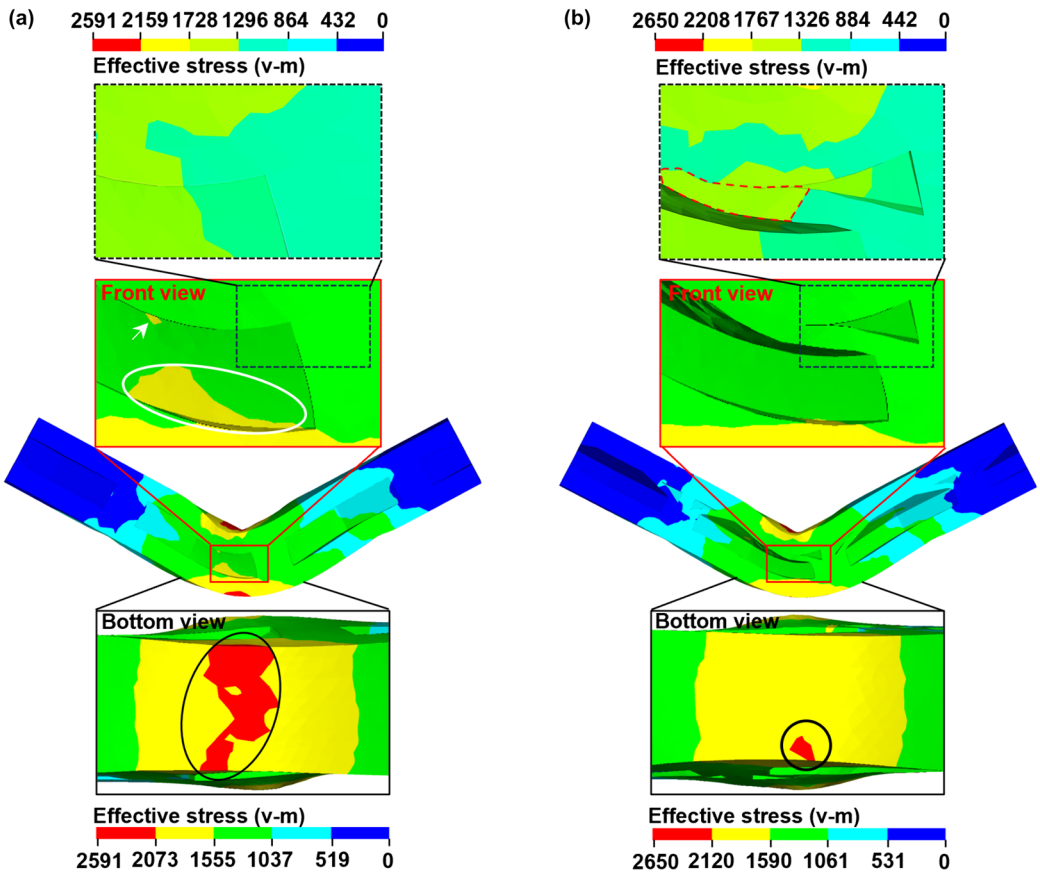

Figure 10 Comparison analysis of stress distribution during bending: (**a**) The 90° structure, (**b**) The 30° structure

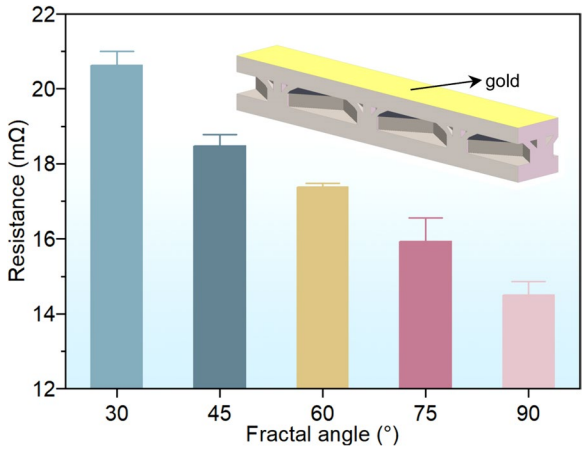

Figure 11 The electrical resistance of LPBF-processed BVHS components

3.4 Electrical Conductivity Properties

The electrical resistance (R), recorded by a DC resistance testing instrument, of the BVHS components with different fractal angles were shown in Figure 11. From the experimental results it can be seen that the resistance decreased with the increase of fractal angle, meaning that higher fractal angle led to better electrical conductivity. It is clear that the fractal angles significantly influence the electrical conductivity properties of the LPBF-processed components.

To better understand the influence mechanism of fractal angles on the electrical conductivity properties of structures, FE simulation was conducted to investigate the current density distributions and the direction of current conduction of different structures at the constant voltage (Figure 12(a)). The length of the arrows indicated the magnitude of the current density and the direction of arrows represented the direction of current conduction. The insets in Figure 12(a) showed structural electrical resistance corresponding to the equivalent circuit. For the 30°, 45° 60° and 75° structures, the honeycomb core consisted of three fractal thin walls and one vertical thin wall, which can be equivalent to three group of parallel resistances (R_1, R_2, R_3) and one electrical resistance (R_4) in series. The equivalent circuit diagram of these four structures was shown in Figure 12(b). For the 90° structure, the honeycomb core only consisted of one vertical thin wall. In order to compare with the electrical resistance of other four structures, the honeycomb core of the 90° structure was divided into two electrical resistances (R_0 and R_4) in series. Figure 12(c) showed the equivalent circuit diagram of the 90° structure. Other electrical

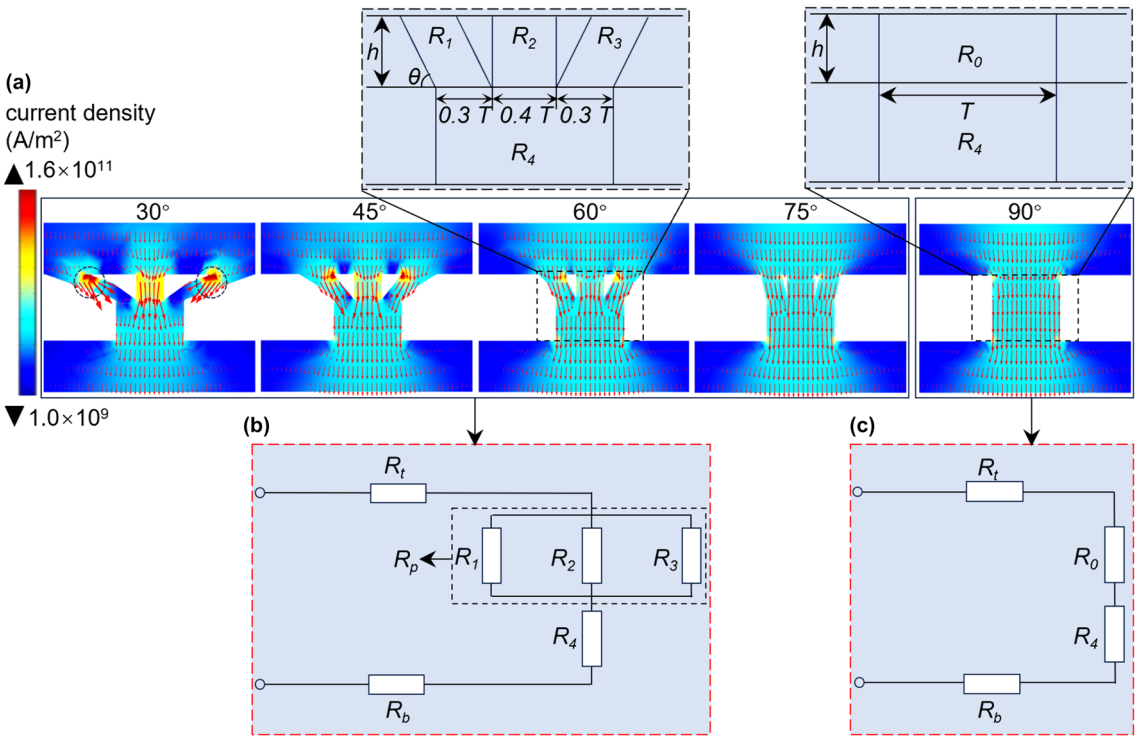

Figure 12 Comparison analysis of current density distribution at a constant voltage and the equivalent circuit diagram: (**a**) The current density distribution of five BVHS structures, (**b**) The equivalent circuit diagram of the 30°, 45°, 60° and 75° structures, (**c**) The equivalent circuit diagram of the 90° structure

resistance, including the top panel, the bottom panel and the sum of three group of parallel resistances were represented as R_t, R_b and R_p, respectively. The relation between the electrical resistance and structure parameters, namely length and cross-section area of current conduction path can be described as follows:

$$R = \rho \frac{L}{S}, \tag{9}$$

where R is the electrical resistance, ρ is resistivity of the material, L is the length of current conduction path, S is cross-sectional area. According to the above equation, R_p and R_0 can be calculated as follows:

$$R_p = \frac{1}{1+\frac{3}{2}\sin^2\theta} \times R_2, \tag{10}$$

$$R_0 = \frac{2}{5} \times R_2, \tag{11}$$

where θ is fractal angle (30°, 45°, 60°, 75°). Comparing the magnitude of R_p and R_0 according to the above equations, it can be seen that R_p is constantly greater than R_0, and R_p decreased with increasing θ. Therefore, the introduction of the fractal feature increased the electrical resistance of the structure, thus negatively affecting the electrical conductivity properties.

In addition, for the 30° structure, it can be clearly observed that the current density concentration occurred at the intersection of fractal thin walls and the top panel (marked by black dashed circle). It can be concluded that due to the introduction of the fractal feature, the current accumulated at the intersection of fractal thin walls and the top panel, and thus reducing the electrical conductivity properties of the structure.

Table 2 Three performance criteria of BVHS components with different fractal angles

Fractal angle (°)	Deviation area (mm^2)	Specific bending strength (MPa/g)	Electrical resistance (mΩ)
30	1.74	238.11	20.63
45	1.53	233.04	18.52
60	1.80	205.96	17.47
75	1.83	200.87	15.51
90	2.54	161.86	14.50

3.5 Design and Optimization of the Powder Outlets

Based on the above study, the overall performance of BVHS structures with different fractal angles were evaluated around three criteria: deviation area, specific bending strength and electrical conductivity. Three performance criteria of BVHS components with different fractal angles were shown in Table 2 and draw in Figure 13(a). Figure 13(b) showed area proportion of the five BVHS structures with different fractal angles. The results showed that the 45° structure had the highest proportion of area, which represented the best overall performance.

When the BVHS structure was applied for LPBF processed sandwich components, un-melted powder would trap inside the enclosed unit cell and can not be removed after LPBF processing. To solve the problem of unmelted powder trapped inside the enclosed unit cells, four unit cells of the 45° structure with different numbers (0, 2, 4 and 6) of self-supported droplet-shaped powder outlets were designed. According to the number of powder outlets, four kinds of unit cells were coded as N_0, N_2, N_4 and N_6. Other structural parameters, including component length, width and height were constantly set as 75 mm, 11 mm, 5 mm, respectively. It is worth noting that a series of 1 mm diameter through holes was designed on

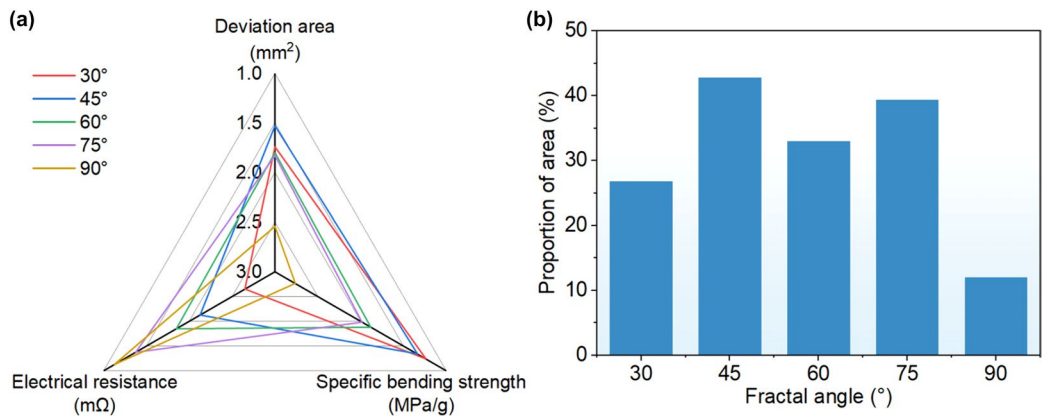

Figure 13 The parameters optimization of the BVHS structure: (**a**) Performance evaluation of BVHS components with different fractal angles based on three performance criteria: deviation area, specific bending strength and electrical resistance, (**b**) Area proportion of the BVHS components

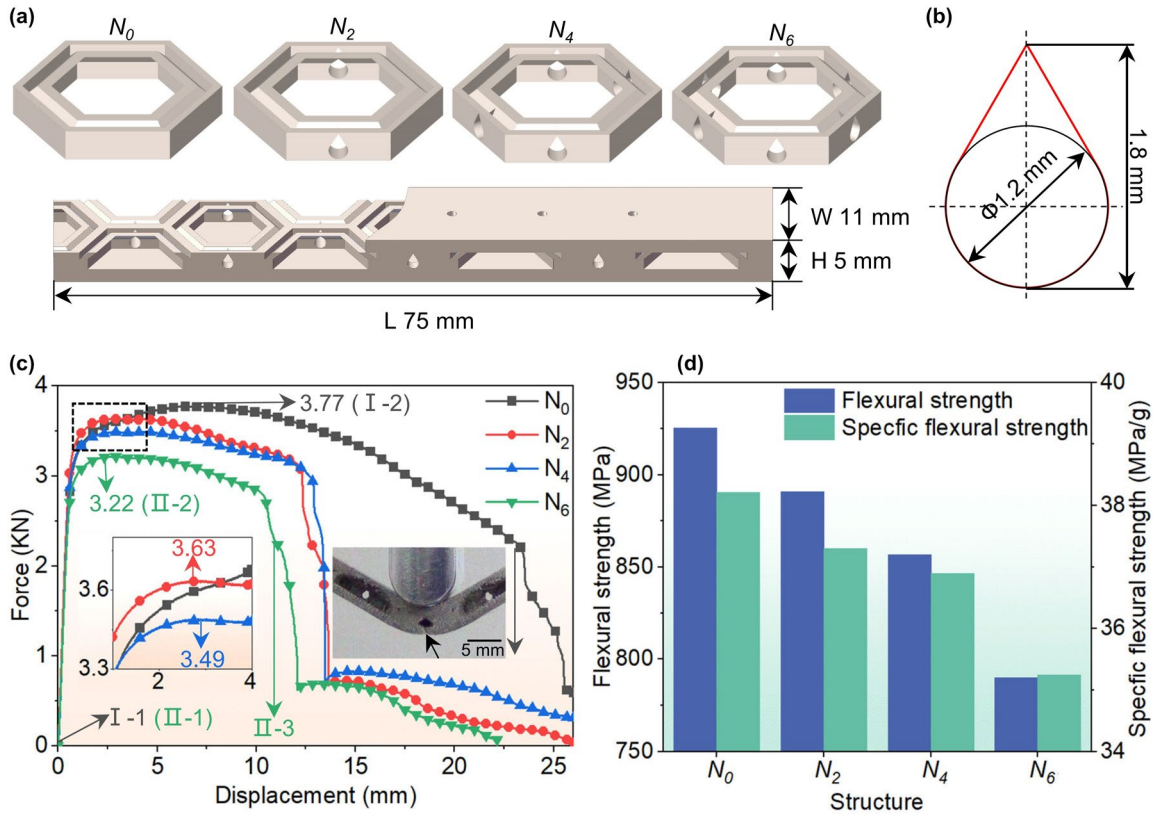

Figure 14 The design and optimization of the powder outlets: (**a**) BVHS with different number of droplet-shaped powder outlets, (**b**) Droplet-shaped geometry of powder outlets, (**c**) Force-displacement bending curves, (**d**) The flexural strength and specific flexural strength of the LPBF-processed 45° component with powder outlets

the top panel of all components, considering powder can get trapped inside the N_0 (Figure 14(a)). Considering that the overhang angle significantly affects the forming quality of LPBF-processed components, the droplet-shaped with self-supporting properties was chosen as the geometry of the powder outlet (Figure 14(b)). LPBF formability improved as the overhang angle increased, so the upper end of the powder outlet consisted of two inclined surfaces with an overhang angle of 60°. In addition, in order to ensure that all the powder in the enclosed unit cells can be removed, the height of the powder outlet must be large enough, but not greater than the height of the core layer (2 mm), so the height of the powder outlet was designed to be 1.8 mm.

After LPBF processing, all BVHS components with different number of powder outlets were ultrasonic cleaned in ethanol for 10 min to well remove trapped powder. The force–displacement curves of four LPBF-processed BVHS components with different number of powder outlets under three-point bending tests were shown in Figure 14(c). It can be seen that the N_0 exhibited the highest ultimate bending force (3.77 kN), which was 3.71%, 7.43%, and 14.59% higher than the N_2 (3.63 kN), the N_4 (3.49 kN) and the N_6 (3.22 kN), respectively. The flexural strength and specific flexural strength of the components were shown in Figure 14(d). With the increase of powder outlets, the specific flexural strength of components decreased from 38.21 MPa to 35.24 MPa, indicating that powder outlets negatively affected bending properties. By observing the deformation processes of components, it was found that the area around the droplet-shaped powder outlets was prone to fracture, which resulted in the reducing of bearing capacity and energy absorption of structures. The inset of Figure 14(c) showed the fracture of N_6 occurred at the bottom end of the powder outlet during bending.

The electrical resistance (R) of BVHS components with powder outlets was measured by a DC resistance testing instrument, and shown in Table 3. It can be seen that the

Table 3 Electrical resistance of components with different number of powder outlets

Strcuture	N_0	N_2	N_4	N_6
R (mΩ)	1.93±0.02	1.81±0.01	1.83±0.01	1.64±0.04

electrical resistance of the N_0 had the highest electrical resistance, was 5.18%, 6.22%, 15.03% than N_4, N_2 and N_6. The results showed that introduction of the powder outlets slightly improved the electrical conductivity properties of components. The possible reason was that the 316L had excellent electrical conductivity properties. Deviations in resistance values mainly caused by other factors during testing, such as interfacial contact resistance and compaction force.

4 Conclusions

In this work, a series of novel bio-inspired vertical honeycomb sandwich (BVHS) structures inspired by the Cybister elytra with different fractal angles were designed and fabricated by LPBF for the application of PEMFC bipolar plates. The influence of the fractal angles on LPBF formability, bending properties and electrical conductivity properties was experimentally investigated, the underlying mechanism was also revealed using FE simulation. Finally, aiming to solve the problem of unmelted powder trapped inside the enclosed unit cells, a self-supported droplet-shaped powder outlet was designed and the number of powder outlets was optimized. The following conclusions can be drawn:

(1) The fractal angles significantly influenced the forming quality of LPBF-processed BVHS components. With the increase of fractal angles, the forming quality of the structures first improved and then deteriorated. The manufacturing accuracy of the 45° component was the best, conversely the 90° component was the worst.

(2) The fractal angles greatly affected the bending properties of structures. With the increase of the fractal angles from 30° to 90°, the ultimate bending load decreased by 32.49%, *SEA* decreased from 10.55 J/g to 6.72 J/g, and specific flexural strength decreased from 238.11 MPa/g to 161.86 MPa/g. The reason was that the introduction of the fractal thin wall obstructed the transmission of force and dissipated most of the force, leading to more uniform distribution of stress across the structure, and thus improving the mechanical properties.

(3) The fractal angles significantly influenced the electrical conductivity properties of the BVHS structures. With the increase of the fractal angles, electrical resistance of the structures decreased from 20.63 mΩ to 14.50 mΩ, meaning that the electrical conductivity properties of the structures gradually improved. Due to the introduction of the fractal feature, the current flow blocked at the intersection of fractal thin walls and the top panel, which resulting in the decrease of current flowing into the bottom panel and thus reducing the electrical conductivity properties of the structure.

(4) The design of droplet-shaped powder outlets negatively affected bending properties of structures. The area around the droplet-shaped powder outlets was more prone to fracture, and with the increase of powder outlet number, the ultimate bending load decreased by 14.59%. However, the design of powder outlets had less impact on the electrical conductivity properties of structures due to the excellent electrical conductivity of the 316L stainless steel.

Acknowledgements
Not applicable.

Authors' Contributions
KL conceived the idea of the study and revised the manuscript; YX conducted most experiment and wrote the manuscript; DG gave advices on the manuscript; SH, KS and WZ were in charge of sampling and laboratory analyses. All authors read and approved the final manuscript.

Funding
Supported by Defense Industrial Technology Development Program of China (Grant No. JCKY2020605C007), Key Research and Development Program of Jiangsu Province of China (Grant Nos. BE2022069, BE2022069-1, BE2022069-3), Aeronautical Science Foundation of China (Grant No. 2020Z049052001).

Availability of Data and Materials
The datasets used and/or analyzed in the current study are available from the corresponding author upon reasonable request.

Declarations

Competing Interests
The authors declare no competing financial interests.

Author Details
[1]College of Materials Science and Technology, Nanjing University of Aeronautics and Astronautics, Nanjing 210016, China. [2]Jiangsu Provincial Research Center for Laser Additive Manufacturing of High-Performance Components, Nanjing 210016, China.

Received: 25 January 2024 Revised: 30 April 2024 Accepted: 1 August 2024
Published online: 12 September 2024

References

[1] A Tang, L Crisci, L Bonville, et al. An overview of bipolar plates in proton exchange membrane fuel cells. *Journal of Renewable and Sustainable Energy*, 2021, 13(2): 022701.
[2] Y Awin, N Dukhan. Metal-foam bipolar plate for PEM fuel cells: Simulations and preliminary results. *Materials Science Forum*, 2018, 933: 342–350.
[3] C W Wu, W Zhang, X Han, et al. A systematic review for structure optimization and clamping load design of large proton exchange membrane fuel cell stack. *Journal of Power Sources*, 2020, 476: 228724.
[4] M Li, L Wu, L Ma, et al. Mechanical response of all-composite pyramidal lattice truss core sandwich structures. *Journal of Materials Science & Technology*, 2011, 27(6): 570–576.
[5] W Yang, J Xiong, L J Feng, et al. Fabrication and mechanical properties of three-dimensional enhanced lattice truss sandwich structures. *Journal of Sandwich Structures & Materials*, 2018, 22(5): 1594–1611.

[6] D W Wang, L Ma, X T Wang, et al. Sound transmission loss of sandwich plate with pyramidal truss cores. *Journal of Sandwich Structures & Materials*, 2018, 22(3): 551–571.
[7] H Liu, Z K Cao, G C Yao, et al. Performance of aluminum foam–steel panel sandwich composites subjected to blast loading. *Materials & Design*, 2013, 47: 483–488.
[8] C He, Y Liu, J Chen, et al. The compressive mechanical properties of honeycomb plates and beetle elytron plates with different foam densities and height-to-thickness ratios. *Journal of Sandwich Structures & Materials*, 2022, 25(3): 372–386.
[9] J P Vitale, G Francucci, A Stocchi. Thermal conductivity of sandwich panels made with synthetic and vegetable fiber vacuum-infused honeycomb cores. *Journal of Sandwich Structures & Materials*, 2016, 19(1): 66–82.
[10] D D Gu, J Yang, K Lin, et al. Compression performance and mechanism of superimposed sine-wave structures fabricated by selective laser melting. *Materials & Design*, 2021, 198: 109291.
11. H Zhou, R Guo, R Liu. Protection properties of stuffed corrugated sandwich structures under hypervelocity impact: Numerical simulation. *Journal of Sandwich Structures & Materials*, 2017, 21(2): 532–551.
[12] S Cai, P Zhang, W Dai, et al. Multi-objective optimization for designing metallic corrugated core sandwich panels under air blast loading. *Journal of Sandwich Structures & Materials*, 2019, 23(4): 1192–1220.
[13] L Meng, J Zhao, X Lan, et al. Multi-objective optimisation of bio-inspired lightweight sandwich structures based on selective laser melting. *Virtual and Physical Prototyping*, 2020, 15(1): 106–119.
[14] N Hao, J Chen, Y Song, et al. A new type of bionic grid plate—The compressive deformation and mechanical properties of the grid beetle elytron plate. *Journal of Sandwich Structures & Materials*, 2021, 24(1): 321–336.
[15] J Bühring, M Nuño, K-U Schröder. Additive manufactured sandwich structures: Mechanical characterization and usage potential in small aircraft. *Aerospace Science and Technology*, 2021, 111: 106548.
[16] C Yan, L Hao, A Hussein, et al. Evaluations of cellular lattice structures manufactured using selective laser melting. *International Journal of Machine Tools and Manufacture*, 2012, 62: 32–38.
[17] A Mitchell, U Lafont, M Hołyńska, et al. Additive manufacturing — A review of 4D printing and future applications. *Additive Manufacturing*, 2018, 24: 606–626.
[18] R Wang, D D Gu, K Lin, et al. Multi-material additive manufacturing of a bio-inspired layered ceramic/metal structure: Formation mechanisms and mechanical properties. *International Journal of Machine Tools and Manufacture*, 2022, 175: 103872.
[19] Y Li, D D Gu, H Zhang, et al. Effect of Trace Addition of Ceramic on Microstructure Development and Mechanical Properties of Selective Laser Melted AlSi10Mg Alloy. *Chinese Journal of Mechanical Engineering*, 2020, 33: 33.
[20] D D Gu, X Shi, R Poprawe, et al. Material-structure-performance integrated laser-metal additive manufacturing. *Science*, 2021, 372(6545): eabg1487.
[21] L Yuan, D D Gu, K Lin, et al. Electrically actuated shape recovery of NiTi components processed by laser powder bed fusion after regulating the dimensional accuracy and phase transformation behavior. *Chinese Journal of Mechanical Engineering: Additive Manufacturing Frontiers*, 2022, 1(4): 100056.
[22] X Cao, B Ji, Y Li, et al. Multi-failure analyses of additively manufactured lattice truss sandwich cylinders. *Composites Part B: Engineering*, 2021, 207: 108561.
[23] Y Wei, C Zhang, Y Yuan, et al. Blast response of additive manufactured Ti–6Al–4V sandwich panels. *International Journal of Impact Engineering*, 2023, 176: 104553.
[24] A Mao, N Zhao, Y Liang, et al. Mechanically efficient cellular materials inspired by cuttlebone. *Advanced Materials*, 2021, 33(15): 2007348.
[25] M Nuño, J Bühring, M N Rao, et al. Delamination testing of AlSi10Mg sandwich structures with pyramidal lattice truss core made by laser powder bed fusion. *Chinese Journal of Mechanical Engineering*, 2021, 34: 126.
[26] L Li, D D Gu, H Liu, et al. Lightweight load-bearing heat dissipation multifunctional pomelo peel-inspired structures fabricated by laser powder bed fusion. *International Journal of Bioprinting*, 2023, 9(6): 413–435.
[27] N S Ha, G Lu. A review of recent research on bio-inspired structures and materials for energy absorption applications. *Composites Part B: Engineering*, 2020, 181: 107496.
[28] J Sun, D D Gu, K Lin, et al. Laser powder bed fusion of diatom frustule inspired bionic NiTi lattice structures: Compressive behavior and shape memory effect. *Smart Materials and Structures*, 2022, 31(7): 074003.
[29] I Ullah, J Elambasseril, M Brandt, et al. Performance of bio-inspired Kagome truss core structures under compression and shear loading. *Composite Structures*, 2014, 118: 294–302.
[30] P Wang, F Yang, G Lu, et al. Anisotropic compression behaviors of bio-inspired modified body-centered cubic lattices validated by additive manufacturing. *Composites Part B: Engineering*, 2022, 234: 109724.
[31] X Wang, R Qin, B Chen. Laser-based additively manufactured bio-inspired crashworthy structure: Energy absorption and collapse behaviour under static and dynamic loadings. *Materials & Design*, 2021, 211: 110128.
[32] J Yang, D D Gu, K Lin, et al. Laser additive manufacturing of bio-inspired metallic structures. *Chinese Journal of Mechanical Engineering: Additive Manufacturing Frontiers*, 2022, 1(1): 100013.
[33] T Maconachie, M Leary, B Lozanovski, et al. SLM lattice structures: Properties, performance, applications and challenges. *Materials & Design*, 2019, 183: 108137.
[34] L Meng, H Liang, H Yu, et al. The energy absorption and bearing capacity of light-weight bio-inspired structures produced by selective laser melting. *Journal of the Mechanical Behavior of Biomedical Materials*, 2019, 93: 170–182.
[35] K Hu, K Lin, D D Gu, et al. Mechanical properties and deformation behavior under compressive loading of selective laser melting processed bio-inspired sandwich structures. *Materials Science and Engineering: A*, 2019, 762: 138089.
[36] S O Obadimu, K I Kourousis. Load-rate effects on the in-plane compressive behaviour of additively manufactured steel 316L honeycomb structures. *Engineering Structures*, 2022, 273: 115063.
[37] N S Ha, G Lu. Thin-walled corrugated structures: A review of crashworthiness designs and energy absorption characteristics. *Thin-Walled Structures*, 2020, 157: 106995.
[38] K Lin, D D Gu, K Hu, et al. Laser powder bed fusion of bio-inspired honeycomb structures: Effect of twist angle on compressive behaviors. *Thin-Walled Structures*, 2021, 159: 107252.
[39] H Xia, Q Sun, S Wang. Influence of strain rate effect on energy absorption characteristics of bio-inspired honeycomb column thin-walled structure under impact loading. *Case Studies in Construction Materials*, 2023, 18: e01761.
[40] S Anandan, R M Hussein, M Spratt, et al. Failure in metal honeycombs manufactured by selective laser melting of 304 L stainless steel under compression. *Virtual and Physical Prototyping*, 2019, 14(2): 114–122.
[41] N Meisel, C Williams. An investigation of key design for additive manufacturing constraints in multimaterial three-dimensional printing. *Journal of Mechanical Design*, 2015, 137(11).
[42] K Lin, J Qiao, K Shi, et al. Laser powder bed fusion of micro-channels for the application of proton exchange membrane fuel cell bipolar plates. *CIRP Journal of Manufacturing Science and Technology*, 2023, 43: 193–204.
[43] Y Wang, F Liu, X Zhang, et al. Cell-size graded sandwich enhances additive manufacturing fidelity and energy absorption. *International Journal of Mechanical Sciences*, 2021, 211: 106798.
[44] R Mertens, S Clijsters, K Kempen, et al. Optimization of scan strategies in selective laser melting of aluminum parts with downfacing areas. *Journal of Manufacturing Science and Engineering*, 2014, 136(6): 061012.

Kaijie Lin born in 1988, is currently an associate professor and a PhD candidate supervisor at *College of Materials Science and Technology, Nanjing University of Aeronautics and Astronautics, China*. His research interests include bio-inspired design for laser additive manufacturing and laser additive manufacturing of high performance metallic components.

Yong Xu born in 1999, is currently a master candidate at *College of Materials Science and Technology, Nanjing University of Aeronautics and Astronautics, China*.

Dongdong Gu born in 1980, is currently a professor and a PhD candidate supervisor at *College of Materials Science and Technology, Nanjing University of Aeronautics and Astronautics, China.* His research

interests include laser additive manufacturing of high-performance/multi-function metallic components.

Junhao Shan born in 1999, is currently a master candidate at *College of Materials Science and Technology, Nanjing University of Aeronautics and Astronautics, China.*

Keyu Shi born in 1999, is currently a PhD candidate at *College of Materials Science and Technology, Nanjing University of Aeronautics and Astronautics, China.*

Wanli Zhang born in 1999, is currently a master candidate at *College of Materials Science and Technology, Nanjing University of Aeronautics and Astronautics, China.*